Label-free imaging of Schwann cell myelination by third harmonic generation microscopy

Hyungsik Lim[a,1], Denis Sharoukhov[a], Imran Kassim[b], Yanqing Zhang[c], James L. Salzer[c], and Carmen V. Melendez-Vasquez[b]

Departments of [a]Physics and [b]Biology, Hunter College of the City University of New York, New York, NY 10065; and [c]Department of Cell Biology and Neurology, New York University School of Medicine, NY 11203

Edited by Ben A. Barres, Stanford University School of Medicine, Stanford, CA, and approved November 11, 2014 (received for review September 15, 2014)

Understanding the dynamic axon–glial cell interaction underlying myelination is hampered by the lack of suitable imaging techniques. Here we demonstrate third harmonic generation microscopy (THGM) for label-free imaging of myelinating Schwann cells in live culture and ex vivo and in vivo tissue. A 3D structure was acquired for a variety of compact and noncompact myelin domains, including juxtaparanodes, Schmidt–Lanterman incisures, and Cajal bands. Other subcellular features of Schwann cells that escape traditional optical microscopies were also visualized. We tested THGM for morphometry of compact myelin. Unlike current methods based on electron microscopy, g-ratio could be determined along an extended length of myelinated fiber in the physiological condition. The precision of THGM-based g-ratio estimation was corroborated in mouse models of hypomyelination. Finally, we demonstrated the feasibility of THGM to monitor morphological changes of myelin during postnatal development and degeneration. The outstanding capabilities of THGM may be useful for elucidation of the mechanism of myelin formation and pathogenesis.

myelin | Schwann cell | multiphoton microscopy | label-free imaging | morphometry

Myelin is a multiple-layered membrane sheath surrounding the axon. In myelinated nerves, the conduction of action potentials is much faster and the speed depends strongly on the structure of myelin. The structural integrity must be therefore tightly regulated for proper conduction of neuronal impulses, but the underlying axon–glial cell interaction is not well understood. Since the days of Ramón y Cajal, light microscopy has been widely used to visualize myelin morphology (1). A variety of fluorescent probes specifically binding to myelin components have allowed studies of the interaction between molecules (2–4). However, most such labeling methods are not suitable for unraveling in vivo dynamics of myelination because cell membranes are compromised during staining (especially immunohistochemistry) and/or the procedures are prohibitively time-consuming and invasive. It is thus of great interest to develop label-free methods. Recently, spectral confocal reflectance microscopy has been demonstrated for high-resolution in vivo imaging of myelin (5). There are also techniques of nonlinear optical microscopy, which are generally known to be more advantageous for imaging deep live tissue. Coherence anti-Stokes Raman scattering (CARS) microscopy, which requires two synchronized short pulse lasers for excitation, has been used for imaging in vivo myelin and detecting pathology (6, 7). Third harmonic generation (THG) microscopy is based on another nonlinear optical process of light emission, yielding distinguishable images from CARS. Though it has been demonstrated for imaging the white matter in the brain (8), so far few studies have applied THG microscopy (THGM) for elucidating the mechanism of myelin formation. Moreover, the omission of the peripheral nervous systems (PNS) in the previous studies is not trivial considering the significant departure from the CNS in terms of the myelin-forming glia and molecular subdomains: Schwann cells wrap individual internodes in the PNS, and oligodendrocytes form multiple myelin sheaths in the CNS. The basal lamina and nodal microvilli are unique to Schwann cells, and Schmidt–Lanterman incisures are more pronounced in the PNS (9). Here we demonstrate, to our knowledge for the first time, the utility of THGM as a method for morphological analysis of myelinating Schwann cells in live culture and ex vivo and in vivo tissue.

Results

Myelin Is the Primary Source of THG Emission. THG emission arises from the myelin sheath due to the discontinuous refractive index at the interface of aqueous media and membrane lipids. Because discontinuity of the same kind exists in the axonal membranes as well, we asked how specific the THG emission is to myelinated vs. unmyelinated axons. To this end, we established myelinating cocultures of dorsal root ganglion (DRG) and Schwann cells. Live-cell THGM imaging was performed at 14 d in vitro (DIV); at this time, cultures contain a mix of myelinated and unmyelinated axons (Fig. 1). The emission showed the optical properties characteristic of THG. The intensity of signal varied when the polarization of excitation beam was rotated, yielding near extinction for orthogonal polarizations relative to the orientation of fibers. THG emission was highly directional, propagating predominantly into the forward direction (or transmission) rather than backward. Sparse elongated segments were observed with lengths between 60 and 160 μm, indicative of myelinating Schwann cells (Fig. 1*A*). The intensity of signal from the myelinated segments was ~5× higher than the background of unmyelinated DRG neurites.

Significance

Myelin, a specialized membrane wrapping around the axon, is crucial for proper neuronal information processing. We describe a label-free imaging method, i.e., third harmonic generation microscopy (THGM), for visualization of Schwann cell myelination in live culture and ex vivo and in vivo tissue. THGM is capable of imaging compact myelin as well as non–compact subcellular domains, including nodal segments, Schmidt–Lanterman incisures, and Cajal bands, thus attractive for elucidating their functional roles; it also facilitates image-based morphometry, allowing the g-ratio of myelinated fibers to be measured in physiological conditions. The demonstrated capabilities of THGM are valuable for investigating the intricate interaction between axon and myelin-forming glial cell underlying formation and maintenance of myelin in the peripheral nervous system.

Author contributions: H.L. and C.V.M.-V. designed research; H.L., D.S., I.K., and C.V.M.-V. performed research; Y.Z. and J.L.S. contributed new reagents/analytic tools; H.L., D.S., and C.V.M.-V. analyzed data; and H.L., J.L.S., and C.V.M.-V. wrote the paper.

The authors declare no conflict of interest.

This article is a PNAS Direct Submission.

[1]To whom correspondence should be addressed. Email: hyungsik.lim@hunter.cuny.edu.

This article contains supporting information online at www.pnas.org/lookup/suppl/doi:10.1073/pnas.1417820111/-/DCSupplemental.

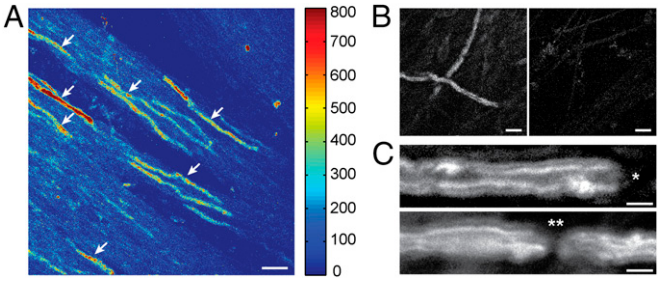

Fig. 1. Live myelinating coculture of rat DRG and Schwann cells imaged by THGM. (*A*) Max projection of z-sections over 15 μm containing several internodes (arrows). (Scale bar, 30 μm.) (*B*) Myelinating coculture (*Left*) vs. DRG only (*Right*). (Scale bars, 10 μm.) (*C*) Localization of heminodes (*) and nodes (**) next to THGM signal from internodes. (Scale bars, 5 μm.)

To confirm that the THG signal indeed originated from myelinated fibers, we prepared two groups of DRG neurons cultured for the same period (2 wk), with or without Schwann cells. The elongated segments emitting strong THG were observed only in the myelinating coculture (Fig. 1*B*), verifying that THG arises from the ensheathed axons and also that the sensitivity of THGM was sufficiently high to detect single myelinating axons. It was also possible to find the locations of heminodes and nodes at the junction of neighboring internodes (Fig. 1*C*). The ability to localize the nascent nodes of Ranvier could be useful for studying the time course of nodal development during myelin formation.

Myelin Subdomains Are Visualized by THGM. Production of THG signal is confined within a tightly focused laser beam, facilitating visualization of the 3D structure of myelinated axons. In our experiments, the theoretical FWHM diameter of the excitation laser focus was 0.4 μm and 1.4 μm in the lateral and axial dimensions, respectively. The high resolution of THGM suggested that it might enable imaging the subcellular structure of myelinated axons. We therefore sought to identify specific subdomains of myelinated peripheral nerves, including the paranodes and Schmidt–Lanterman incisures. We used transgenic mice whose myelin domains were labeled with fluorescent proteins expressed under specific promoters; coregistration of simultaneously acquired two-photon excited fluorescence (TPEF) and THG permitted definitive identification of the THG features. To make the identification more evident, we used isolated myelinated axons obtained from teasing fresh sciatic nerves. All data presented in this report were acquired without fixation. The first transgenic mouse used was a Rosa26-mT/mG (10), a reporter line that expresses tandem dimer Tomato (tdTomato) at axonal and glial cell membranes. Substantial overlap of tdTomato and THG signals was found along the continuous membranes, verifying the membranes as the origin of THG (Fig. 2 *A* and *B*). The lateral resolution of THGM was sufficiently high to discriminate the adaxonal (inner) and abaxonal (outer) membranes of compact myelin. Schmidt–Lanterman incisures were observable in both tdTomato and THG channels (Fig. 2*A*, arrowheads), whereas the nodal axolemma was detected only as an interrupted THG lining (Fig. 2*B*, arrow). To validate the localization of the nodes with respect to the THG signal, we used a transgenic mouse expressing neurofascin 186 (NF186), a nodal cell-adhesion molecule, tagged with EGFP and expressed under the control of *Thy-1.2* promoter (11). The myelinated axons of the NF186 animal showed that EGFP signal was diffuse and weak around Schmidt–Lanterman incisures where NF186 do not cluster (Fig. 2*C*), but strong EGFP fluorescence arising from the nodal axolemma coincided with the gap in THGM, confirming that the node of Ranvier is located at the interrupted THG membranes (Fig. 2*D*). These results show that THGM is capable of distinguishing major domains such as the nodes and incisures.

The spatial resolution of THGM was further tested for visualizing the detailed morphology of subdomains using freshly isolated sciatic nerves of rat. By virtue of the depth-sectioning capability of THGM, 3D structure of subdomains could be acquired. Substantial anatomical diversity was displayed at the incisures and nodes. A representative image of the node of Ranvier is presented in Fig. 3 with volumetric rendering reconstructed from a z-stack of images (Fig. 3*A*). The paranodal loops were only partially visualized, and the nodal axolemma was not visible (Fig. 3*B*). The adaxonal and abaxonal membranes were clearly resolved in the lateral (*xy*) section but not in the axial section (*xz*) of the fiber due to the asymmetric lateral and axial resolutions. The cross-sections through the node exhibited gradual shifts from concentric circles in compact myelin (Fig. 3*C*, *a* and *j*) to undulating contours in the juxtaparanode (Fig. 3*C*, *b*, *c*, *h*, and *i*). We observed on occasion spiral paranodal loops reminiscent of the helical distribution of Caspr (contactin-associated protein) in the juxtaparanode, which has been interpreted to reflect preservation of the spiraled apposition of these loops to the axon during myelin growth (12). Next we studied the Schmidt–Lanterman incisures (Fig. 3*D*). The classic funnel shape, familiar from previous electron and light microscopy (13, 14), had an inclination angle of ~10° (Fig. 3*E*). The axon was significantly constricted at Schmidt–Lanterman incisures with the diameter reduced to ~60% level. The cross-section of Schmidt–Lanterman incisures showed concurrent tapering and thinning of sheath as well as shifting of cytoplasmic channels across the myelin sheath (Fig. 3*F*).

There are also other subcellular features revealed by THGM that do not normally appear in traditional microscopies. For instance, the lamellae dividing cytoplasmic channels within the incisures, which are not visible under immunohistochemistry against myelin-associated glycoprotein (MAG), showed that their orientation was nearly perpendicular to that of the adjacent myelin (Fig. 3*G*). The large contortion requires large mechanical strains imposed on the membranes, and thus indicates the significant role of junctions and the associated adhesion molecules, such as E-cadherin, in maintaining structural integrity of the incisures (15–17).

Quantification of Myelin Morphology. It is possible to take advantage of the unique imaging contrast of THGM for precise quantification of myelin morphology. To demonstrate THGM-based morphometry, we decided to examine a principal metric of myelinated nerves, i.e., the g-ratio, which is the ratio of axon diameter to that of total fiber. A substantial deviation from a g-ratio value of ~0.7 is indicative of abnormal myelination (18). THGM was performed on fresh rat sciatic nerves. The epineurium was removed to release the individual fibers for modest separation, but the nerve was otherwise intact. The backscattered THG signal was collected by epidetection

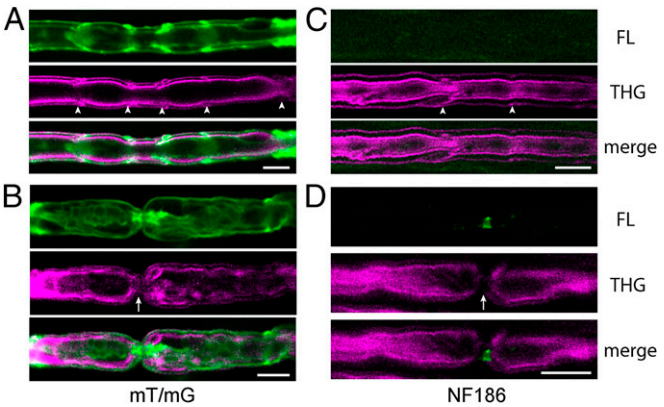

Fig. 2. Identification of node and incisures by coregistration of simultaneously acquired fluorescence (FL, green) and THG (magenta) in freshly isolated teased fibers. (*A* and *B*) Membrane-targeted (mT/mG) and (*C* and *D*) NF186-EGFP transgenic mice. Myelin domains are clearly identifiable in THG images: Incisures (arrowheads) and nodes (arrows) are indicated. (Scale bars, 20 μm.)

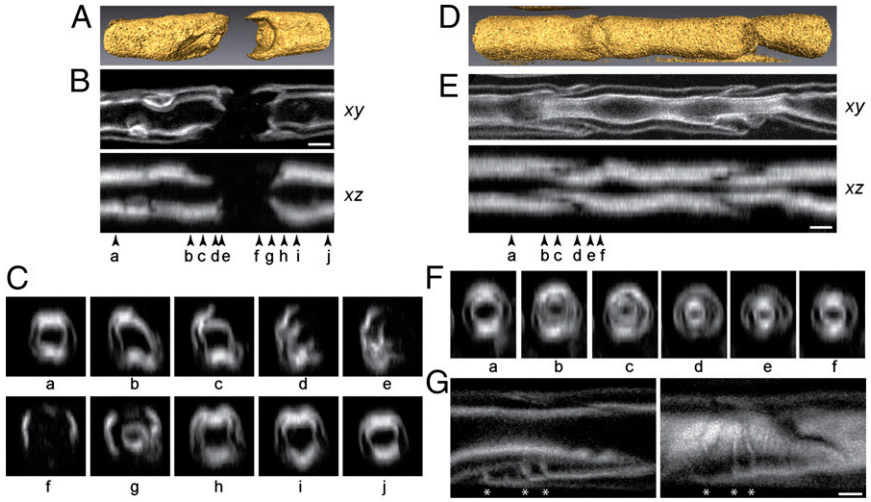

Fig. 3. Three-dimensional structure of domains in fresh teased adult rat sciatic nerve. (*A*) Volumetric rendering of nodal segment. (*B*) The lateral (*xy*) and longitudinal (*xz*) sections. (Scale bar, 3 μm.) (*C*) Ten cross-sections (*a–j*) at the positions marked by arrowheads in *A*. (*D*) Volumetric rendering of Schmidt–Lanterman incisure. (*E*) The lateral (*xy*) and longitudinal (*xz*) sections. (Scale bar, 5 μm.) (*F*) The cross-sections (*yz*) at the positions marked by arrowheads in *E*. Axon constriction at the incisure is apparent. (*G*) The cytochannel walls (*) in the middle of the nerve fiber (*Left*) and 3 μm above (*Right*). (Scale bar, 3 μm.)

(Fig. 4*A*). Evaluation of g-ratio was straightforward due to a characteristic of THG process. The generation of THG signal was localized at the interface between lipid and aqueous solution so that the boundaries of axon and myelin sheath could be easily identified by sharp peaks in the THG intensity profile (Fig. 4*B*). From the diameters of axon and fiber, the g-ratio was determined in a precise and unbiased manner. The estimated value for the profile in Fig. 4*B* was 0.67. The large field of view of THGM is desirable for mapping the g-ratio over an extended segment of single fiber. The ease with which the longitudinal profile of g-ratio can be determined without laborious sectioning as in serial block-face EM (19) would be a great advantage for large-scale quantitative analysis of the myelin distribution in 3D tissue (20). We measured myelin thickness along a single axon (Fig. 4*C*). Interestingly, the thickness of myelin sheath was relatively uniform, suggesting a constant number of wrapping and an interlamellar spacing throughout the length of axon. Because the diameter of axon was not as conserved, the proportionality between myelin and axon was only approximate on the microscopic scale, and as a consequence there were considerable variations in the g-ratio (~5%) even within a single internode. Understanding the variability of the metric may be important not only for detecting the onset of pathologies but also as a possible mechanism to modulate the conduction of action potentials.

The precision and the range of THGM-based morphometry were examined in detail. Two animal models of hypomyelination were used along with WT: knockout mice haploinsufficient for NRG1 type III (*NRG1 type III*$^{+/-}$) and trembler Tr-J with a heterozygous point mutation in the *PMP22* gene (*Pmp22*$^{Tr\text{-}J}$). NRG1 type III is a transmembrane protein expressed by the axons that is crucial for determining their ensheathment fate; haploinsufficiency of NRG1 type III results in hypomyelination (21, 22). PMP22 is a major component of PNS compact myelin, and the mutant displays severe hypomyelination (23, 24). We examined freshly teased sciatic nerves from the corresponding adult mice. As expected, THGM could detect hypomyelination in the nerve fibers isolated from Tr-J and *NRG1 type III*$^{+/-}$ mice compared with WT (Fig. 4*D*). Tr-J mice also exhibited other morphological anomalies (Fig. S1), including nonuniform myelin thickness across the internode due to incomplete compaction and a failure to convert mesaxon to compact myelin. The thickness of myelin in Tr-J mice was too small to measure the g-ratio, and only the lower bound could be determined ($g > 0.80$). To compare WT and *NRG1 type III*$^{+/-}$ mice, we measured g-ratios at various locations sufficiently away from noncompact domains along the sciatic nerves (Fig. 4*E*; four animals per each genotype). The g-ratio of *NRG1 type III*$^{+/-}$ mice was significantly higher than that

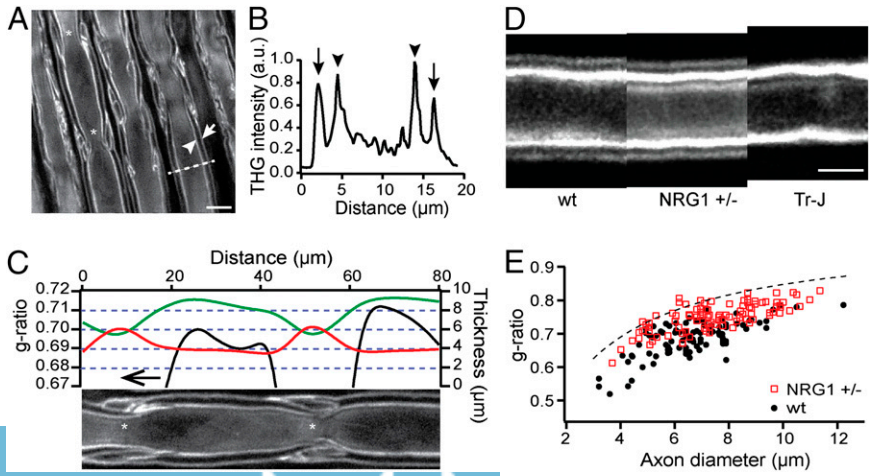

Fig. 4. Ex vivo morphometry of myelin sheath by THGM. (*A*) Lateral section of fresh, nonteased rat sciatic nerve showing the adaxonal (arrowhead) and abaxonal (arrow) membranes. (Scale bars, 10 μm.) (*B*) Intensity profile for the dashed line in *A* showing the positions of the adaxonal (arrowhead) and abaxonal (arrow) membranes. The corresponding g-ratio is 0.67. (*C*) The thickness of axon (green) and myelin sheath (red), and the g-ratio (black) along the internode shown at the bottom. (*D*) Unfixed, teased sciatic nerves of WT, *NRG1 type III*$^{+/-}$, and Tr-J mice with similar caliber. The position of the abaxonal membrane shifts because of the difference in myelin thickness. (Scale bar, 5 μm.) (*E*) The scatter plot of g-ratio as a function of axon caliber in WT and *NRG1 type III*$^{+/-}$ animals (a total of 100 axons from $n = 4$ animals per genotype). The dashed line denotes the g-ratio in case of 0.9-μm gap between the adaxonal and abaxonal membranes.

of WT (0.75 ± 0.005 vs. 0.69 ± 0.01, mean ± SEM; $P = 0.0016$, t test), which is consistent with the previous EM measurements (21). The result verifies the capability of THGM-based morphometry to detect modest hypomyelination. The measured g-ratio was lower for axons of smaller calibers, which could be due to a limit in the measurement imposed by the resolution of THGM. The g-ratio could not be evaluated when the spacing between the adaxonal and abaxonal boundaries is much smaller than the optical resolution, resulting in underestimation of the parameter more significant for thinner axons. The upper bound for the measured g-ratio values corresponded to ∼0.9-μm spacing (dashed line in Fig. 4*E*). The apparent limit in the measurable myelin thickness was a little larger than the FWHM diameter of the diffraction-limited focus, presumably because of degradation in the resolution due to specimen-induced optical aberrations.

Imaging Intact Nerves ex Vivo and in Vivo. Substantial merit is expected from using THGM imaging for studying the dynamics of Schwann cell myelination in vivo. However, in order for THGM to be applicable to intact in vivo nerves, the images must be taken by epidetection of THG signal. Though THG radiation is predominantly forward-propagating, epidetection THGM imaging has been achieved for thick specimen because turbid surrounding medium causes significant backward-scattering of THG (25). We examined whether the effect is sufficiently strong that myelinated axons could be imaged in intact excised tissues as well as in live animals. First, nonteased excised sciatic nerves were imaged by simultaneous second harmonic generation (SHG) and THG imaging. Indeed myelinated fibers were visualized by epidetection THGM while collagenous endoneurium and perineurium were simultaneously recorded via SHG signal excited by the same laser beam (Fig. 5*A*). The node of Ranvier and Schmidt–Lanterman incisures were clearly identified in the high-resolution views (Fig. 5 *B* and *C*). Furthermore, Cajal bands and appositions could be also detected on the surface of myelin sheath (arrows and arrowheads in Fig. 5*D*, respectively). The ability to image these domains in intact nerves is attractive for elucidating their functional roles (26). We tested the feasibility of THGM-based g-ratio measurement for intact tissues. The g-ratio was evaluated for all of the available fibers shown in Fig. 5 *B* and *C*, and the average g-ratio was 0.62 (Fig. 5*F*). Once it was established that THGM images of intact nerves ex vivo could be acquired, we then performed in vivo THGM imaging of sciatic nerve using live mice. Although the brightness of the images obtained was comparable to the ex vivo conditions, the resolution of imaging was degraded by motion artifacts, and subcellular details could not be resolved even with image registration (Fig. 5*G*). The movement of nerves as much as a few micrometers per second, especially in the axial direction, was sufficient to confound g-ratio analysis. Nevertheless, it was possible to visualize nodes and incisures in living mice (Fig. 5*G*, arrow). Suitable methods to immobilize in vivo tissue could further improve the overall image quality.

Imaging Postnatal Growth and Pathological Myelin. We examined the utility of THGM for studying developing myelin. Rat sciatic nerves were harvested from animals ($n = 3$) at P2, P4, P6, P11, and P18, and imaged by THGM. The most noticeable change occurring between P2 and P4 was that the majority of axons become myelinated (Fig. S1*A*). Interestingly, the sparsely distributed internodes at P2 were already substantially long at this early age (∼100 μm), much as in myelinating DRG coculture systems (Fig. 1*A*), implying that the Schwann cell extends quickly after initial decision to myelinate the axon. Other distinctive changes were compaction of myelin sheath and formation of nodes. The width of internode became uniform across the fiber at P4, and compact myelin was common throughout the nerve at P6 (Fig. S1*B*). During this period, many individual fibers (10–20% of the imaged internodes) still contained noncompact regions along the internode, and some of the bulbs remained even after P6 (Fig. S1*C*, arrowheads). As the number of internodes increased, more gaps emerged as presumptive nodes of Ranvier (Fig. S1*D*, arrows). By P11, the sciatic nerves contained nodes and incisures that resembled those of adult animals. A majority of nodes had mature appearance at P11, and fully developed incisures were readily observable at P18. These results suggest THGM as a promising technique to image myelinogenesis in situ, which has been primarily studied by EM (27).

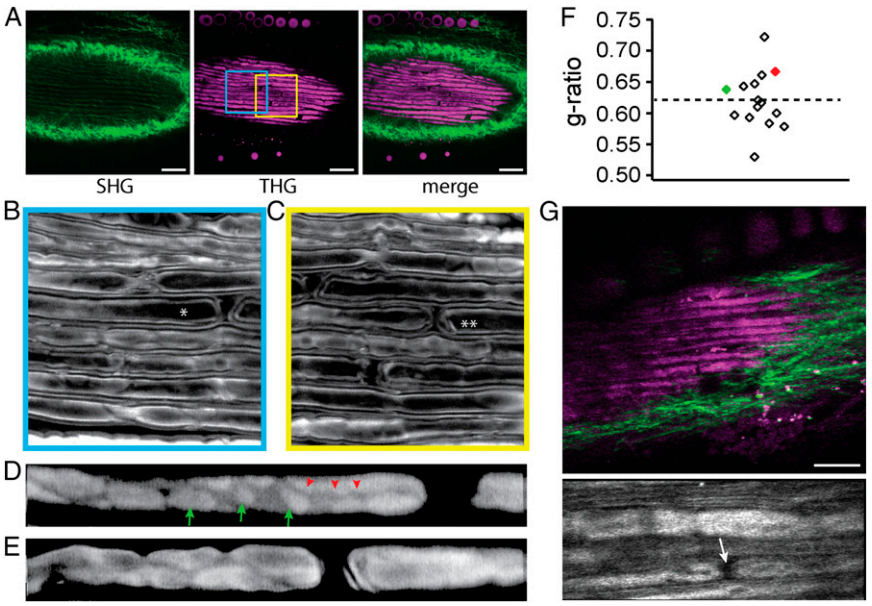

Fig. 5. Imaging-intact murine sciatic nerves ex vivo and in vivo. (*A*) Simultaneous SHG and THG imaging of ex vivo tissue. (Scale bar, 50 μm.) (*B* and *C*) Regions corresponding to the colored frames in *A*. The axons marked by asterisk (*) and double asterisks (**) are shown at higher magnification in *D* and *E*, respectively, focused at the level of the abaxonal membrane. Cajal bands (red arrowheads) and appositions (green arrows) are visible. The images of *D* and *E* are displayed on logarithmic intensity scales for easier identification. (*F*) The g-ratio of the fibers shown in *B* and *C*. Red and green points correspond to the marked fibers in *B* and *C*, respectively. (*G*) Imaging of in vivo tissue. (Scale bar, 30 μm.) (*Lower*) High-magnification view containing a node (arrow).

We also studied whether THGM can detect demyelination. To model demyelination in vitro, we treated myelinating cocultures at 14 d after ascorbate addition with glial growth factor (GGF; 200 ng/mL), an isoform of neuregulin 1 known to induce demyelination (28). As a control, a group of cells was cultured for the same periods without GGF treatment. Cells imaged with THGM after 3 and 7 d of GGF treatment are depicted in Fig. S2 *D* and *E*, respectively. Various patterns of deformation were visible in the cells affected by GGF, which confirms that the origin of THG is the myelin sheath. Disrupted myelin sheaths were prominent after 3 d, and extensive demyelination was apparent after 7 d.

Discussion

Electron and light microscopy have long been the methods of choice for visualizing myelin morphology (9). Myelin structures pertaining to physiology, from the interlamellar spacing to the internode length, cannot be captured by a single technique because the dimension spans over seven orders of magnitude. Moreover, even a single nerve bundle contains hundreds of axons confounding the determination of a microscopic biometric (e.g., the g-ratio) for a population of peripheral nerves. The submicrometer resolution and wide field of view (~1 mm^2) of THGM facilitates rapid surveillance of compact and noncompact myelin subdomains over many internodes, and also any gradient from proximal to distal nerves relative to the spinal cord. Examination of peripheral nerves could be greatly simplified by means of label-free THGM avoiding elaborate procedures for fixation, labeling, or embedding. The removal of fixation and disruptive staining, as well as the freedom from photobleaching, is crucial for studying the native dynamics of myelin formation and impairment in live cells.

We have shown that THG signal is specific to myelin sheath and provides a previously unidentified imaging contrast for visualizing diverse myelin domains in living animals, including Schmidt–Lanterman incisures, node of Ranvier, and Cajal bands. The demonstrated capability is highly beneficial for investigating the in vivo dynamics of domains. We have also shown the utility of THG for estimation of g-ratio. The current method of g-ratio measurement is based on EM sections lacking 3D spatial relationship, so the parameter is evaluated only at a single point along the axon. To overcome the limitation and also to make g-ratio estimation more convenient, alternative methods using light microscopy have been developed but with limited success. The use of Luxol fast blue stain in conjunction with wide-field microscopy does not yield accurate results. CARS microscopy was demonstrated for evaluation of g-ratio (6). However, the identification of axon and fiber boundaries is ambiguous, requiring an arbitrary definition of myelin thickness because CARS signal arises from the bulk of the myelin sheath. Recently developed spectral confocal reflectance microscopy is inadequate for precise determination of g-ratio because the reflection occurs primarily at the top and bottom surfaces of myelin sheath (5). By contrast, THGM images the entire axial sections (Fig. 3) and the sensitivity to the interfaces enables unambiguous and bias-free evaluation of the g-ratio. The demonstrated g-ratio measurement relies on peak detection, a computationally cheap and robust process, so it is amenable to automated morphometric analysis. Furthermore, the longitudinal map of g-ratio can be acquired without having to prepare thin sections. Using THGM morphometry, we have found significant variations in g-ratio within a single internode.

Although pseudocrystalline compact myelin is conducive to quantitative analysis, the whole myelin structure, including noncompact domains, cannot be characterized by any one metric, including the g-ratio. Conceivably, THGM imaging could aid in devising a new metric that reflects the subcellular complexity of myelin. Consider as an example the angle of Schmidt–Lanterman incisures. The noncompact domain has been depicted in an unrolled myelin sheath as obliquely traversing channels relative to the axon (14, 29). This view suggests that the angle of incisures is related to the tilt of channel. However, a rudimentary calculation shows that the angle between the channel and axon is nearly 90° and does not account for the angle of incisures. Here, a relation is derived following the Cajal's laws of conservation (30) for the angle of incisures to optimize both the width of channels and the outer diameter of fiber. From a geometrical model of the incisures (Fig. 6), we obtain

$$\frac{T+\alpha}{\sin\theta} = T + w \cdot N = T + w \cdot \frac{T}{d},$$

where T is the thickness of myelin, α is the axonal constriction, θ is the angle of incisures, N is the number of wrapping, w is the width of cytoplasmic channel, and d is the thickness of single lamella (~17 nm). Assuming the axonal constriction is linearly proportional to the thickness of myelin ($\alpha = \varepsilon T$), the width of cytoplasmic channel is given as

$$w = \left(\frac{1+\varepsilon}{\sin\theta} - 1\right) \cdot d.$$

For typical values of axonal constriction ($\varepsilon = 0.6$) and the angle of incisures (θ = 10 degrees), the equation yields the channel width of 140 nm, which is consistent with the values measured by EM (31); it indicates that the width of cytoplasmic channel, which may be a relevant indicator for the domain's function, is maintained by a balance between the axonal constriction and the incisures angle. More importantly, the channel width, which is smaller than the diffraction-limited optical resolution, can be predicted from the measurable quantities of THGM, i.e., the angle of incisures and the orientation of the dividing lamellae (Fig. 3*G*).

Methods

Third Harmonic Generation Microcopy. We used an experimental setup for THGM similar to the described in the literature (32–34). Short pulses from an optical parametric oscillator (OPO) were used to excite THG. The OPO was pumped with a mode-locked Ti:Sapphire laser (Chameleon Ultra; Coherent, Inc.) with a pulse duration of 100 fs at an 80-MHz repetition rate. The center wavelength of OPO output was 1,180 nm. The polarization of excitation laser light was adjusted with a half- or quarter-wave plate. A water-dipping microscope objective lens with high N.A. focused the laser beam (Olympus XLUMPlanFL 20× 1.0 N.A. or Nikon CFI75 16× 0.8 N.A.). For epidetection of THG signal from intact in vivo and ex vivo nerves (Figs. 4*A* and 5), the same objective lens collected backward-scattered THG, which was then recorded with a photomultiplier tube (PMT; Hamamatsu H7422-40). For THGM imaging of live cells and teased nerve fibers, forward-propagating THG signal was collected and detected in a transmission setup consisting of a high-N.A. objective lens (Olympus UApo340 40× 1.35 N.A.), a narrowband spectral filter (Chroma), and a PMT (Hamamatsu H10492-003). Both forward and backward detection used nondescanned mode. The average power $\langle P \rangle$ at the sample was ~20–50 mW and the pixel dwell time was ~4 μs. Images were averaged over three frames. For in vivo imaging, 5–10 frames were individually acquired without averaging at the frame rate of ~2 Hz.

Simultaneous THGM and Two-Photon Microscopy Imaging. Other light emissions were simultaneously acquired for coregistration with myelin THG. SHG signal visualized collagenous connective tissue, i.e., endoneurium and

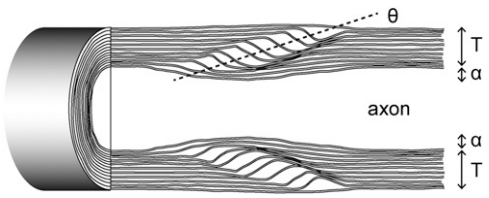

Fig. 6. Schematic illustration of the Schmidt–Lanterman incisures showing structural parameters for THGM-based quantitative analysis.

perineurium, whereas TPEF from EGFP and tdTomato revealed subcellular features. SHG was excited by the same OPO output beam as THG and detected after a narrowband spectral filter at half the excitation wavelength (λ = 590 nm). For TPEF, a separate mode-locked Ti:Sapphire laser (Tsunami; Spectra-Physics, Inc.) was used with the excitation wavelength at 850 nm and 880 nm for EGFP and tdTomato, respectively. For simultaneous THGM and TPEF imaging, the laser beam was combined into the optical path using a dichroic filter (Chroma 950DC). The SHG and TPEF signals were acquired by epidetection.

Image Processing and Quantification of Myelin. Myelin morphology was quantified via image processing using ImageJ (National Institutes of Health) and MATLAB (MathWorks, Inc.). Volumetric reconstruction was created using Amira (VSG). For estimation of g-ratio, automatic peak detection was performed on THG intensity profile across myelinated axon to objectively determine the boundaries of the myelin sheath. G-ratio was calculated from the obtained diameters of fiber and axon. Statistical analyses of the measured g-ratio were performed using Prism (GraphPad, Inc.). Density of myelin during postnatal growth was quantified. At each time point, a total of six nerve regions of interest (ROIs) with an area of 114 × 114 μm^2 were selected from three animals. Each ROI was converted into a binary image by automatic thresholding, which distinguished myelin from nonmyelin. The density of myelin was obtained by counting the number of nonzero pixels and then averaging over six ROIs.

Animals. Sprague–Dawley rats were obtained from Charles River Laboratories. Transgenic mT/mG [*Gt(ROSA)26Sor*$^{tm4(ACTB-tdTomato,-EGFP)}$] and myelin mutant trembler (*Pmp22*$^{Tr-J}$) mice were obtained from Jackson Laboratories.

Myelinating Schwann Cell Culture for Live Cell Imaging. Myelinating coculture system was prepared as described (35). DRG neurons were isolated from E16 rat spinal cords and maintained in serum-free neurobasal (NB) medium (2% B27 supplement, 2 mM L-glutamine, 0.4% glucose, and 50 ng/mL 2.5S NGF). Nonneuronal cells were removed by feeding the cultures with NB medium containing 5-fluorodeoxyuridine and uridine. Schwann cells were isolated from postnatal day 2 sciatic and expanded for ~3 wk in D media (10% FBS, and 2 mM L-glutamine) supplemented with 4 μM forskolin and 5 ng/mL of the EGF domain of rhNRG-1-β1 (R&D Systems). Myelinating cocultures were established by seeding purified DRG neuron cultures with 100,000 Schwann cells in C media (10% FBS, 2 mM L-glutamine, 0.4% glucose, and 50 ng/mL 2.5S NGF). After 3 d, cocultures were changed to media supplemented with 50 μg/mL ascorbic acid to initiate basal lamina formation and myelination. For demyelination experiment mature myelinating cocultures (14–21 d) were treated with GGF (200 ng/mL) for 2–7 d, a treatment that is known to cause demyelination in vitro (28).

Preparation of Teased Nerve Fiber. Sciatic nerves were harvested from mice and rats of specified ages. Fresh (unfixed) sciatic nerves were teased using fine needles in ice-cold Dulbecco's PBS. The teased nerve fibers were then transferred to a glass-bottom dish (MatTek) and held down with a slice anchor (Warner Instruments) for imaging.

Animal Surgery for in Vivo Imaging. Animal surgery for in vivo imaging of sciatic nerves was performed as previously described (5, 36, 37). The procedure was approved by the Hunter College Institutional Animal Care and Use Committee. Animals were anesthetized by isoflurane inhalation and placed on a temperature-controlled heating pad. The hind leg was shaved and sterilized with betadine. A small incision was made on the skin. The vastus lateralis and biceps femoris muscles were separated using retractors. The sciatic nerve was exposed and gently lifted with a thin spatula introduced underneath the nerve. The position of spatula was adjusted using a micromanipulator (Narishige) to orient the sciatic nerve relative to the excitation laser beam and to mitigate breathing artifacts. After imaging, the animal was euthanized.

ACKNOWLEDGMENTS. We thank Tomasz Rusielewicz and Matt Urbanski for help with preparation of the sciatic nerve samples. This work was funded by National Institutes of Health Grants GM096884 and MD007599 (to H.L.), NS26001 (to J.L.S.), and NS000001 (to C.M.-V.).

1. Ramón y Cajal S (1991) *Degeneration and Regeneration of the Nervous System* (Oxford Univ Press, London).
2. Condie AG, Gerson SL, Miller RH, Wang Y (2012) Two-photon fluorescent imaging of myelination in the spinal cord. *ChemMedChem* 7(12):2194–2203.
3. Romanelli E, et al. (2013) Cellular, subcellular and functional in vivo labeling of the spinal cord using vital dyes. *Nat Protoc* 8(3):481–490.
4. Reynolds RJ, Little GJ, Lin M, Heath JW (1994) Imaging myelinated nerve fibres by confocal fluorescence microscopy: Individual fibres in whole nerve trunks traced through multiple consecutive internodes. *J Neurocytol* 23(9):555–564.
5. Schain AJ, Hill RA, Grutzendler J (2014) Label-free in vivo imaging of myelinated axons in health and disease with spectral confocal reflectance microscopy. *Nat Med* 20(4):443–449.
6. Wang H, Fu Y, Zickmund P, Shi R, Cheng JX (2005) Coherent anti-stokes Raman scattering imaging of axonal myelin in live spinal tissues. *Biophys J* 89(1):581–591.
7. Bélanger E, et al. (2012) Live animal myelin histomorphometry of the spinal cord with video-rate multimodal nonlinear microendoscopy. *J Biomed Opt* 17(2):021107.
8. Farrar MJ, Wise FW, Fetcho JR, Schaffer CB (2011) In vivo imaging of myelin in the vertebrate central nervous system using third harmonic generation microscopy. *Biophys J* 100(5):1362–1371.
9. Peters A, Palay SL, Webster HD (1991) *Fine Structure of the Nervous System: Neurons and Their Supporting Cells* (Oxford Univ Press, London).
10. Muzumdar MD, Tasic B, Miyamichi K, Li L, Luo L (2007) A global double-fluorescent Cre reporter mouse. *Genesis* 45(9):593–605.
11. Zhang Y, et al. (2012) Assembly and maintenance of nodes of ranvier rely on distinct sources of proteins and targeting mechanisms. *Neuron* 73(1):92–107.
12. Pedraza L, Huang JK, Colman D (2009) Disposition of axonal caspr with respect to glial cell membranes: Implications for the process of myelination. *J Neurosci Res* 87(15): 3480–3491.
13. Bunge MB, Bunge RP, Peterson ER, Murray MR (1967) A light and electron microscope study of long-term organized cultures of rat dorsal root ganglia. *J Cell Biol* 32(2): 439–466.
14. Ghabriel MN, Allt G (1981) Incisures of Schmidt–Lanterman. *Prog Neurobiol* 17(1-2): 25–58.
15. Fannon AM, et al. (1995) Novel E-cadherin-mediated adhesion in peripheral nerve: Schwann cell architecture is stabilized by autotypic adherens junctions. *J Cell Biol* 129(1):189–202.
16. Poliak S, Matlis S, Ullmer C, Scherer SS, Peles E (2002) Distinct claudins and associated PDZ proteins form different autotypic tight junctions in myelinating Schwann cells. *J Cell Biol* 159(2):361–372.
17. Tricaud N, Perrin-Tricaud C, Brusés JL, Rutishauser U (2005) Adherens junctions in myelinating Schwann cells stabilize Schmidt–Lanterman incisures via recruitment of p120 catenin to E-cadherin. *J Neurosci* 25(13):3259–3269.
18. Lazzarini RA (2004) *Myelin Biology and Disorders* (Elsevier, San Diego).
19. Denk W, Horstmann H (2004) Serial block-face scanning electron microscopy to reconstruct three-dimensional tissue nanostructure. *PLoS Biol* 2(11):e329.
20. Tomassy GS, et al. (2014) Distinct profiles of myelin distribution along single axons of pyramidal neurons in the neocortex. *Science* 344(6181):319–324.
21. Taveggia C, et al. (2005) Neuregulin-1 type III determines the ensheathment fate of axons. *Neuron* 47(5):681–694.
22. Michailov GV, et al. (2004) Axonal neuregulin-1 regulates myelin sheath thickness. *Science* 304(5671):700–703.
23. Suter U, et al. (1992) Trembler mouse carries a point mutation in a myelin gene. *Nature* 356(6366):241–244.
24. Notterpek L, Shooter EM, Snipes GJ (1997) Upregulation of the endosomal-lysosomal pathway in the trembler-J neuropathy. *J Neurosci* 17(11):4190–4200.
25. Débarre D, Olivier N, Beaurepaire E (2007) Signal epidetection in third-harmonic generation microscopy of turbid media. *Opt Express* 15(14):8913–8924.
26. Court FA, et al. (2004) Restricted growth of Schwann cells lacking Cajal bands slows conduction in myelinated nerves. *Nature* 431(7005):191–195.
27. Webster HD (1971) The geometry of peripheral myelin sheaths during their formation and growth in rat sciatic nerves. *J Cell Biol* 48(2):348–367.
28. Zanazzi G, et al. (2001) Glial growth factor/neuregulin inhibits Schwann cell myelination and induces demyelination. *J Cell Biol* 152(6):1289–1299.
29. Arroyo EJ, Scherer SS (2000) On the molecular architecture of myelinated fibers. *Histochem Cell Biol* 113(1):1–18.
30. Ramón y Cajal S (1995) *Histology of the Nervous System of Man and Vertebrates* (Oxford Univ Press, London).
31. Hall SM, Williams PL (1970) Studies on the "incisures" of Schmidt and Lanterman. *J Cell Sci* 6(3):767–791.
32. Yelin D, Silberberg Y (1999) Laser scanning third-harmonic-generation microscopy in biology. *Opt Express* 5(8):169–175.
33. Squier J, Muller M, Brakenhoff G, Wilson KR (1998) Third harmonic generation microscopy. *Opt Express* 3(9):315–324.
34. Débarre D, et al. (2006) Imaging lipid bodies in cells and tissues using third-harmonic generation microscopy. *Nat Methods* 3(1):47–53.
35. Einheber S, et al. (1997) The axonal membrane protein Caspr, a homologue of neurexin IV, is a component of the septate-like paranodal junctions that assemble during myelination. *J Cell Biol* 139(6):1495–1506.
36. Williams PL, Hall SM (1970) In vivo observations on mature myelinated nerve fibres of the mouse. *J Anat* 107(Pt 1):31–38.
37. Gonzalez S, Fernando RN, Perrin-Tricaud C, Tricaud N (2014) In vivo introduction of transgenes into mouse sciatic nerve cells in situ using viral vectors. *Nat Protoc* 9(5): 1160–1169.